CHEMISTRY OF MATERIALS

pubs.acs.org/cm

Article

A First-Principles Explanation of the Luminescent Line Shape of $SrLiAl_3N_4:Eu^{2+}$ Phosphor for Light-Emitting Diode Applications

Julien Bouquiaux,* Samuel Poncé, Yongchao Jia, Anna Miglio, Masayoshi Mikami, and Xavier Gonze

Cite This: *Chem. Mater.* 2023, 35, 5353−5361

Read Online

ACCESS | Metrics & More | Article Recommendations | Supporting Information

ABSTRACT: White light-emitting diodes are gaining popularity and are set to become the most common light source in the U.S. by 2025. However, their performance is still limited by the lack of an efficient red-emitting component with a narrow band emission. The red phosphor $SrLiAl_3N_4:Eu^{2+}$ is among the first promising phosphors with a small bandwidth for next-generation lighting, but the microscopic origin of this narrow emission remains elusive. In the present work, density functional theory, the ΔSCF-constrained occupation method, and a generalized Huang−Rhys theory are used to provide an accurate description of the vibronic processes occurring at the two Sr^{2+} sites that the Eu^{2+} activator can occupy. The emission band shape of Eu(Sr1), with a zero-phonon line at 1.906 eV and a high luminescence intensity, is shown to be controlled by the coupling between the $5d_{z^2}$−4f electronic transition and the low-frequency phonon modes associated with the Sr and Eu displacements along the Sr channel. The good agreement between our computations and experimental results allows us to provide a structural assignment of the observed total spectrum. By computing explicitly the effect of the thermal expansion on zero-phonon line energies, the agreement is extended to the temperature-dependent spectrum. These results provide insight into the electron−phonon coupling that accompanies the 5d−4f transition in similar UCr_4C_4-type phosphors. Furthermore, these results highlight the importance of the Sr channel in shaping the narrow emission of $SrLiAl_3N_4:Eu^{2+}$, and they shed new light on the structure−property relations of such phosphors.

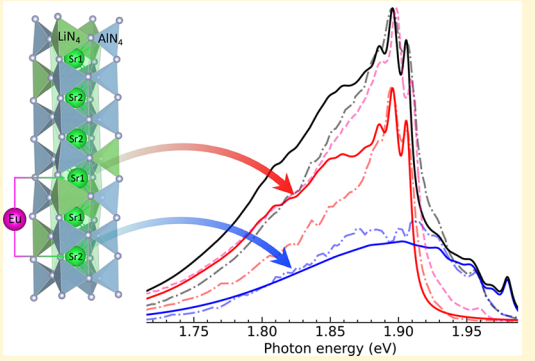

INTRODUCTION

Eco-efficient white light-emitting diodes (WLEDs) rely on one or more phosphor materials to convert the ultraviolet or blue emission from an LED chip into the desired wavelength emission spectrum. Phosphors are made of a host material doped with an activator, the latter which emits light whose wavelength is tuned by the effect of the host's crystal structure and chemical environment. The numerous combinations between host and activator have led to the creation of thousands of possible phosphor materials with a variety of photoluminescence (PL) properties, including emission peak wavelength, thermal stability, quantum efficiency, and shape of the PL emission spectrum. In the past decade, a large focus has been put on the discovery of phosphors with narrow emission bandwidth in order to improve the color purity of backlighting LED devices or, in the case of the red phosphors in WLED, to avoid wasting energy in the near-infrared region where the human eye is not sensitive.[1−3]

In the search for new-generation phosphors,[4] materials with a UCr_4C_4-type structure doped with Eu^{2+} have recently attracted attention.[5,6] The first instance of such materials, the $SrLiAl_3N_4:Eu^{2+}$ (SLA) phosphor, discovered by Schnick et al.,[7] was quickly followed by other nitride-based phosphors such as $Sr[Mg_2Al_2N_4]:Eu^{2+}$ and $Sr[Mg_3SiN_4]:Eu^{2+}$.[8,9] Given the strong nephelauxetic effect of the N_8 cuboid environment around the Eu activator, the emission color was limited to the red region. To lower the emission wavelength while still maintaining performance similar to that of SLA, O^{2-} was added to the cuboid environment, like in oxy-nitride $Sr[Li_2Al_2O_2N_2]:Eu^{2+}$ (SALON),[10] to allow blue shifting of the emission peak from 650 nm (SLA) to 614 nm. Numerous oxide-based phosphors were then developed with the general formula $M_4[Li_3SiO_4]_4$, where M can be selected from Li^+, Na^+, K^+, Rb^+, Cs^+, and their combinations.[5,11,12] Most of these alkali lithosilicate phosphors with an O_8 cuboid environment provide green-cyan-blue emission.

It is commonly accepted that the narrow band emission of the Eu-doped UCr_4C_4 structure is linked to the highly condensed host structure and the cuboid coordination environment. However, the microscopic origin of such narrow emission is not fully understood. In this respect, Huang−Rhys theory[13] and its generalization,[14,15] fed by first-principles

Received: March 9, 2023
Revised: June 26, 2023
Published: July 6, 2023

computations, allows one to gain insight into the electron−phonon coupling that accompanies electronic optical transitions. Mainly used in the context of defects for quantum information technologies,[15−18] this theory was only exploited recently to obtain information on the phonon sidebands of a few selected phosphors.[19−21]

Despite the pioneer status and technological relevance of SLA,[22] its phonon sidebands with apparent vibronic signatures have not yet received any theoretical attention. Initial theoretical studies of SLA focused only on the bulk host material.[23,24] Recently, a time-dependent density functional theory (DFT) approach for embedded clusters has clarified the electronic processes responsible for light absorption in SLA, but it has not investigated emission or the PL spectrum.[25]

In SLA, the europium dopant can substitute for the strontium atom in two inequivalent positions, which lead to two emission centers. Thanks to their different decay time, time-resolved luminescence was used in 2016 to decompose the zero-phonon lines (ZPLs) for these two centers, 15377 cm^{-1} (1.906 eV) and 15780 cm^{-1} (1.956 eV), and the corresponding phonon sideband of each center; however, their structural assignment was not done.[26]

In this work, we study from first principles the vibronic processes occurring in the PL spectrum of the $SrLiAl_3N_4:Eu^{2+}$ (SLA) phosphor. We simulate the PL spectra from the two luminescent sites and assign them to their specific microscopic environment using predictive methods whose accuracies have been demonstrated previously.[27−31]

We use large supercells computed with DFT and the ΔSCF-constrained method to obtain optimized Eu 4f ground state structures and Eu 5d excited state structures. The atomic displacements induced by the 5d−4f transitions are projected onto the phonon modes of the system in order to obtain the Huang−Rhys (HR) spectral function, which provides information on the nature of the phonons participating in the transition. The HR spectral function is converged by increasing the supercell size by using the embedding procedure proposed by Alkauskas et al.[14] The PL line shape is computed following the generating function approach and its temperature-dependent generalization.[15] Finally, the effect of thermal expansion on PL properties is included via volumetric quasi-harmonic approximation (QHA)[32,33] with a minimization of the Helmholtz free energy with respect to the global volume. This allows one to estimate ZPL energies with increasing temperatures.

It is found that the emission line shape with a ZPL energy around 1.906 eV and a very narrow emission bandwidth[26] is associated with the Sr site having a second coordination sphere composed of 3 Li and 5 Al; the emission line shape with the higher ZPL energy of around 1.956 eV and a larger emission bandwidth is associated with the Sr site having a second coordination sphere composed of 1 Li and 7 Al. The very distinct shapes of the two PL spectra originate from different promoted excited 5d orbitals ($5d_{z^2}$-like aligned along the Sr channel and $5d_{x^2-y^2}$-like pointed along Al/Li atoms), which lead to different 5d−4f atomic relaxation patterns and hence different electron−phonon coupling. By explicitly including the effect of thermal expansion on the ZPL energies, inducing a blue shift of around 30 meV for both sites between 10 and 573 K, we find an excellent agreement between the simulated and experimental temperature-dependent PL spectra.

The paper is structured as follows. We first present the theoretical background and computational methodology. The results of the work are then presented. Both Sr sites are compared carefully for each of the following properties: the excited state geometry, the coupling with phonons, and the temperature-dependent PL spectra, including thermal expansion effects. Finally, we provide additional discussions and conclude this work.

THEORY AND COMPUTATIONAL METHODOLOGY

Huang−Rhys Theory for the Luminescence Spectrum. Within the Huang−Rhys theory and the Franck−Condon approximation,[13,34] ground state (GS) and excited state (ES) potential energy surfaces are projected along the harmonic phonon normal coordinates of the system Q_ν. The GS and ES surfaces are assumed to be identical (same phonon frequencies ω_ν and eigenmodes) except for a rigid offset ΔQ_ν coming from a linear electron−phonon interaction and an energy difference called the zero-phonon line energy E^{ZPL}. This reduces the problem to a displaced harmonic oscillator problem for each phonon mode ν, as depicted in Figure 1,

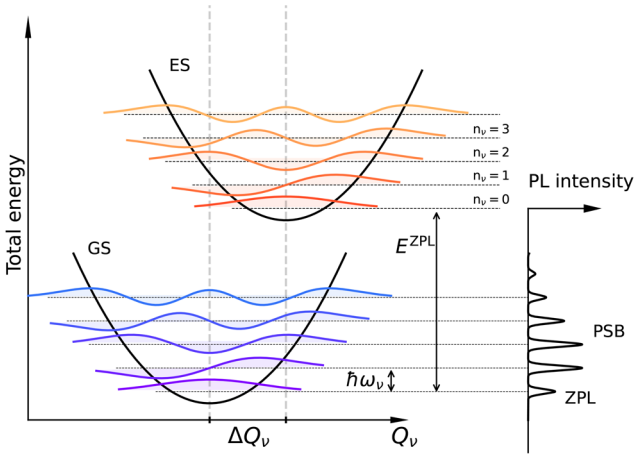

Figure 1. Schematic representation of the origin of the photoluminescence (PL) spectra. On the left, ground state (GS) and excited state (ES) energy curves are projected along phonon normal coordinate Q_ν (here only for one mode) and are approximated by harmonic functions with the same frequency ω_ν. Vibrational energy levels and corresponding eigenfunctions are shown as horizontal lines and colored areas. GS and ES are displaced by ΔQ_ν, the mass-weighted displacement between the minimum of the GS and ES curves. On the right, the PL spectrum is formed. The zero-phonon line (ZPL) comes from the transition between the first vibrational level of the ES to the first vibrational level of the GS. Other transitions give the phonon sideband (PSB). The intensity of each peak is computed with the overlap between corresponding eigenfunctions.

for which an analytic expression to compute the associated phonon sideband (PSB) exists. At 0 K, where only the ES vibrational state $n = 0$ contributes, one has $|\langle\chi_{n_\nu}^{GS}|\chi_{0_\nu}^{ES}\rangle|^2 = e^{-S_\nu}(S_\nu)^{n_\nu}/(n_\nu!)$ with S_ν being the Huang−Rhys factor of mode ν. For a given photon energy $\hbar\omega$, the luminescence intensity is given by[14,15,20]

$$L(\hbar\omega, T) \propto \omega^3 A(\hbar\omega, T) \quad (1)$$

where the line shape function $A(\hbar\omega)$ is evaluated as the Fourier transform of the generating function $G(t, T)$:[35]

$$A(\hbar\omega, T) = \int_{-\infty}^{+\infty} G(t, T) e^{i\omega t - \frac{\gamma}{\hbar}|t| - i\frac{E^{ZPL}}{\hbar}t}\, dt \quad (2)$$

$$G(t, T) = e^{S(t) - S(0) + C(t,T) + C(-t,T) - 2C(0,T)} \quad (3)$$

https://doi.org/10.1021/acs.chemmater.3c00537
Chem. Mater. 2023, 35, 5353−5361

where $S(t) = \sum_\nu S_\nu e^{i\omega_\nu t}$ and $C(t, T) = \sum_\nu \overline{n}_\nu(T) S_\nu e^{i\omega_\nu t}$ are the Fourier transforms of the Huang−Rhys spectral functions and the temperature-weighted Huang−Rhys spectral functions, respectively. γ is the homogeneous Lorentzian broadening of each vibronic transition, and $\overline{n}_\nu(T)$ is the average occupation number of the νth phonon mode:

$$\overline{n}_\nu(T) = \frac{1}{e^{\hbar\omega_\nu/k_B T} - 1} \tag{4}$$

The components of eq 2 are the partial Huang−Rhys factor of each phonon mode S_ν, the phonon frequencies ω_ν, and the zero-phonon line energy E^{ZPL}. The S_ν is the mean number of phonon ν involved in the transition:

$$S_\nu = \frac{\frac{1}{2}\omega_\nu^2 \Delta Q_\nu^2}{\hbar\omega_\nu} = \frac{\omega_\nu \Delta Q_\nu^2}{2\hbar} \tag{5}$$

where ΔQ_ν is the mass-weighted atomic displacement projected along phonon mode ν

$$\Delta Q_\nu = \sum_{\kappa\alpha} \sqrt{M_\kappa}\, \Delta R_{\kappa\alpha} e_{\nu,\kappa\alpha} \tag{6}$$

Here, $\mathbf{\Delta R}_\kappa = \mathbf{R}_\kappa^{GS} - \mathbf{R}_\kappa^{ES}$ is the vector associated with the displacement of atom κ between the excited and ground state, $\mathbf{e}_{\nu,\kappa}$ are the phonon eigenvectors, and M_κ are the atomic masses. Under the harmonic approximation, eq 6 becomes

$$\Delta Q_\nu = \frac{1}{\omega_\nu^2} \sum_{\kappa\alpha} \frac{\Delta F_{\kappa\alpha} e_{\nu,\kappa\alpha}}{\sqrt{M_\kappa}} \tag{7}$$

where $\mathbf{\Delta F}_\kappa$ are the ground state forces evaluated at the equilibrium excited state structure. This formulation is advantageous, as the forces decay faster than the displacements (see Sections 1.1 and 1.2 of the Supporting Information (SI)).[36] We use DFT to obtain the ground state optimized structure $\mathbf{R}_\kappa^{GS}$, the forces $\mathbf{\Delta F}_\kappa$, the phonon eigenvectors $\mathbf{e}_{\nu,\kappa}$, and the eigenfrequencies ω_ν. The ΔSCF-constrained occupation method is used to optimize the excited state structure, $\mathbf{R}_\kappa^{ES}$.

Computational Method. Calculations are performed with DFT using ABINIT[37,38] with the PAW method.[39] The generalized gradient approximation (GGA-PBE) is used to treat exchange-correlation effects[40] and a Hubbard U = 7 eV term is added on the 4f states of europium, as is consistent with our previous works.[29] We find that the value of the U parameter has only a weak impact on the ZPL energy and the 5d−4f displacements, as seen in Section 2 of the SI.[36] Calculations on Eu-doped SLA are conducted with a 2 × 2 × 2 supercell containing 288 atoms. The two possible emission centers are treated as two independent systems. For all supercell calculations, the structures are relaxed below a maximal residual force of 10^{-4} hartree/bohr (about 0.005 eV/Å). The cutoff kinetic energy is 25 hartrees (680 eV) with a single zone-centered **k**-point. For the treatment of the Eu $4f^6 5d^1$ excited state, we use the ΔSCF method wherein the eigenfunctions associated with the highest predominantly Eu 4f band are forced to be unoccupied while the next predominantly Eu 5d energy band is constrained to be occupied. While the latter is more hybridized than the Eu 4f band, it is nevertheless referred to as a Eu 5d band. The ZPL energy is computed as the difference between the total energy of the relaxed excited states and that of the ground state. Detailed information on the use of this approach can be found in ref 19. This work focuses on the lowest excited state of the $4f^6 5d^1$ configuration and describes the vibronic features appearing in the emission spectrum of the two emission centers. The complete $4f^6 5d^1$ configuration, giving rise to a complex fine structure in the excitation band, cannot be captured with our methodology. Multiconfigurational methods for embedded-cluster[41,42] are more suitable to understand the $4f^6 5d^1$ manifold and the absorption spectra of Eu-doped phosphor materials.

Phonons and Embedding Methodology. Phonon modes of the undoped primitive cell of SLA containing 36 atoms are obtained by diagonalizing the dynamical matrices computed with density functional perturbation theory (DFPT) with a 2 × 2 × 2 **k**-points and **q**-points grid and then Fourier interpolated on a fine 4 × 4 × 4 **q**-grid.[43] The phonon band structure is Fourier interpolated along high-symmetry lines, and the density of states can be found in Section 3 of the SI.[36]

Reaching the dilute limit requires the estimation of the interatomic force constants (IFCs) on large defective supercells, which would be computationally too expensive with a direct approach. Hence, a technique similar to the one proposed by Alkauskas et al.[14] is followed. The IFCs of the pristine SLA, computed on a 4 × 4 × 4 **q**-grid, are mapped on the corresponding 4 × 4 × 4 supercell. The IFCs of the Eu-doped system are computed on a smaller 2 × 2 × 2 supercell containing 288 atoms using a frozen-phonon approach as implemented in the PHONOPY package.[44] In order to construct the total IFCs, the following cutoff is applied. If both atoms κ and κ' are separated from the dopant by a distance smaller than R_c = 5.5 Å, then the IFCs computed with the 2 × 2 × 2 defect supercell are used. For all other atomic pairs, the IFCs computed with the pristine system are used. This procedure breaks the acoustic sum rule,[15] which we reimpose with $C_{\kappa\alpha,\kappa\alpha} = -\sum_{\alpha\neq\beta} C_{\kappa\beta,\kappa\alpha}$, where α and β refer to the Cartesian coordinates. This embedding methodology allows one to obtain the phonon eigenfrequencies ω_ν and the eigenvectors $\mathbf{e}_{\nu,\kappa}$ of eq 7 on the 4 × 4 × 4 supercell. The forces $\mathbf{\Delta F}_\kappa$ of eq 7 are those of the 2 × 2 × 2 supercell and are set to zero elsewhere because of the short-range decay of the forces with respect to the Eu activator. Convergence of the Huang−Rhys spectral function as a function of the size of the large supercell is reported in Section 1.3 of the SI.[36]

Thermal Expansion. To compute the effect of thermal expansion, the volumetric quasi-harmonic approximation (QHA) is used, neglecting deviatoric thermal stresses and internal forces (v-ZSISA approximation).[45−47] The only contributions to the thermal expansion of the crystal are the coupling between phonons and the change in unit cell volume,[48] with cell parameters and internal coordinates relaxed at fixed volumes. We obtain the temperature versus volume curve of the undoped SLA by minimizing the Helmholtz free energy (FE)[32,33,49]

$$F(V, T) = E(V) + F^{vib}(V, T) \tag{8}$$

where

$$F^{vib}(V, T) = \sum_{\mathbf{q}\nu} \frac{\hbar\omega_{\mathbf{q}\nu}(V)}{2} + k_B T \ln(1 - e^{-\hbar\omega_{\mathbf{q}\nu}(V)/k_B T}) \tag{9}$$

Here, $E(V)$ is the static DFT energy versus volume curve, with all non-volumetric degrees of freedom relaxed, and $F^{vib}(V, T)$ is the vibration energy with the same cell and atomic geometry. The FE curve is constructed using seven configurations within a [−2%, +4%] volume change with respect to the static equilibrium volume. The minimum volume for a given temperature is obtained by fitting a Murnaghan equation of state[50] to the FE curve. Detailed information on the FE curves, the temperature-dependent thermal expansion coefficient, and zero-point volume are reported in Section 4 of the SI.[36] To evaluate the effect of thermal expansion on the PL spectrum, we have scaled the lattice parameters obtained for the undoped SLA to the 288 atoms supercells and recomputed the ZPL energies at fixed volumes corresponding to the selected temperatures (see Figure S8 of the SI).[36] This allowed us to compute both the shift of the ZPL energies with temperature and the effect zero-point volume has on the ZPL energies at 0 K.

RESULTS AND DISCUSSION

Ground State Geometry. The SLA crystallizes in a triclinic crystal system ($P\bar{1}$ space group) with the typical channel structure observed in other UCr_4C_4-type phosphors; see Figure 2.

Our computed lattice parameters are overestimated by about 0.3%, which is common for PBE exchange and correlation

https://doi.org/10.1021/acs.chemmater.3c00537
Chem. Mater. 2023, 35, 5353−5361

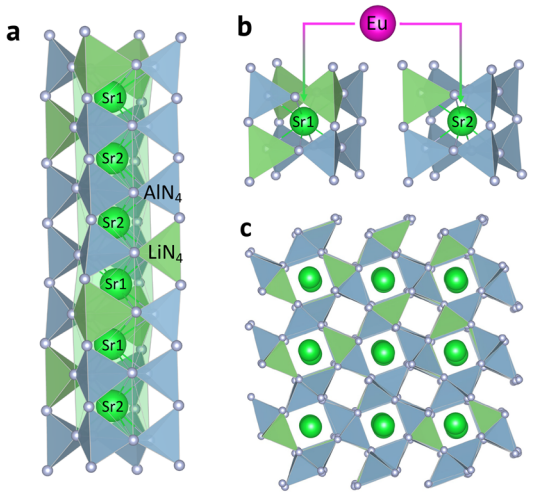

Figure 2. (a) Crystal structure of $SrLiAl_3N_4:Eu^{2+}$ viewed along the Sr chain. (b) First- and second-shell environments of Sr1 and Sr2 sites where the Eu atom can substitute. (c) Structure perpendicular to the Sr chains with the characteristic UCr_4C_4 framework.

functionals. The angles match within a 0.05° difference. Half of the channels are occupied by the Sr^{2+} ions. These channels are built up with an ordered tetrahedral alignment, as seen in Figure 2a, with one green $[LiN_4]^{11-}$ followed by three blue $[AlN_4]^{9-}$. Two Sr sites with a very similar first shell environment ($Sr-N_8$) but a different second shell can host the Eu activator and are shown in Figure 2b, which leads to two emission centers. The first site, denoted as Sr1 in this work, is surrounded by 3 $[LiN_4]^{11-}$ and 5 $[AlN_4]^{9-}$ tetrahedra, while the second, denoted as Sr2, is surrounded by 1 $[LiN_4]^{11-}$ and 7 $[AlN_4]^{9-}$ tetrahedra. We observe that within the Sr chain, the Sr1−Sr1 distance of 3.2 Å is shorter than the Sr2−Sr2 distance of 3.42 Å. The Sr1−Sr2 distance is in-between, with a value of 3.28 Å. We compute that the $Sr-N_8$ cuboid has similar mean Sr−N distances in both sites (2.809 and 2.804 Å). When the Sr atoms are replaced by Eu atoms, these distances change by less than 0.1% due to similar atomic radii for the Eu^{2+} and Sr^{2+} atoms.[51] Additional information can be found in Section 5 of the SI.[36]

Excited State Geometry. The probability densities of the highest occupied Kohn−Sham orbitals associated with the $4f^7$ ($^8S_{7/2}$) ground and lowest $4f^6$ (^7F_J) $5d^1$ excited states are presented in Figure 3a and b for both Sr sites. The computed energy levels are reported in Section 6 of the SI.[36] In a hypothetical pure cubic EuN_8 environment, $5d_{z^2}$ and $5d_{x^2-y^2}$ would be the lowest degenerate d-states. However, this degeneracy is lifted when considering a nonperfect EuN_8 cuboid with a different second-shell environment ($[LiN_4]^{11-}$ and $[AlN_4]^{9-}$ tetrahedra) and different Eu−Sr distances along the 1D Sr chain.

In the case of Eu(Sr1), we observe that a $5d_{z^2}$-like orbital is stabilized along the Sr chain, as in the case of $Sr-[Li_2Al_2O_2N_2]:Eu^{2+}$.[19] The $5d_{x^2-y^2}$-like state is also located in the band gap, but 0.27 eV above the $5d_{z^2}$-like state.

In contrast, for Eu(Sr2), the opposite situation appears: a $5d_{x^2-y^2}$-like orbital is stabilized, perpendicular to the Sr chain. The four lobes point toward the interstitial area of the low electrostatic potential produced by the nitrogen ligands. The inversion of the 5d states' ordering appears to be related to the difference in second-shell environments, given the similarity of the $Eu-N_8$ cuboids. However, it is unclear whether the inversion is caused by the difference in Eu−Sr distances (steric effect) or by the difference in the types of tetrahedra (Coulombic effect). To explore this further, we relaxed a fictitious system in which the Eu atom replaces Sr1 while keeping the Eu−Sr distances fixed at the relaxed Eu(Sr2) values. Our findings indicate that the $5d_{z^2}$ state remains stabilized, but the $5d_{x^2-y^2}$ state is now 0.15 eV above it. This suggests that the difference in tetrahedra types is the primary explanation for the inversion of the 5d states with some contribution from the difference in Eu−Sr distances.

We stress that in ref 25, it was argued that the similar local geometry and electronic structure between the two sites lead to a similar emission spectrum. However, our computations

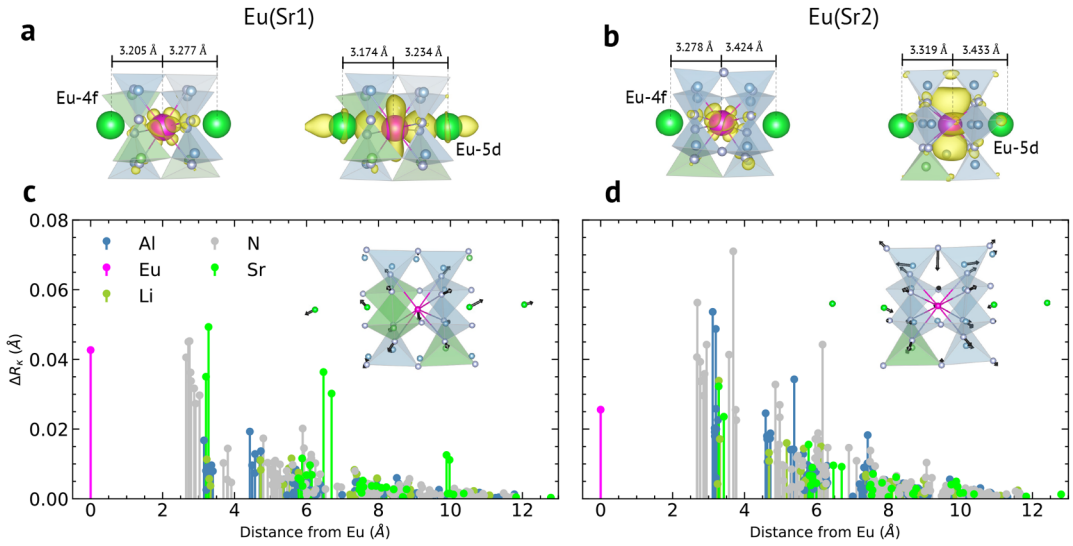

Figure 3. Probability density of the highest occupied Kohn−Sham orbitals associated with the $4f^7$ ($^8S_{7/2}$) ground and lowest $4f^6$ (^7F_J) $5d^1$ excited states for the (a) Eu(Sr1) and (b) Eu(Sr2) sites. Norm of the atomic displacements induced by the 5d−4f transition (upon emission) for the (c) Eu(Sr1) site and (d) Eu(Sr2) site as a function of the distance from Eu. The insets show a three-dimensional view of these displacements near the Eu activator, scaled by 20 for clarity.

https://doi.org/10.1021/acs.chemmater.3c00537
Chem. Mater. 2023, 35, 5353−5361

contradict this claim, as we have found that the two sites possess different electronic structures that result in distinct emission spectra, as will be demonstrated later on. We also find that for both sites, the computed energy separation between the empty 5d state and the conduction bottom (Sr-4d character) is 0.29 eV. Experimentally, the 5d conduction band separation is estimated to be 0.28 eV[24] based on a fitting of thermal quenching data with an exponential nonradiative decay rate from the 5d state to the conduction bottom through thermal excitation. Despite the good agreement between these values, it is important to remember that the Kohn−Sham energy levels calculated using GGA-PBE are only approximations of the actual energy levels, and this agreement should be appreciated with caution.

The displacement fields associated with the 5d−4f transition are presented in the insets of Figure 3c and d, scaled by 20 for clarity. The norm of these displacements is shown as a function of the distance from the Eu activator. For both Sr sites, upon emission, going from the 5d to the 4f state leads to an elongation of Eu−N bond lengths by 0.03−0.06 Å. Indeed, upon 5d excitation, additional covalent interactions appear between the N ligands with the inner 4f hole that shortens the bond length.[41] Interestingly, the Eu atom moves in its cuboid cage as a result of its nonsymmetrical environment. Looking now at the atomic rearrangements beyond the first coordination shell, we see first that a significant fraction of the total displacements is outside this first shell, as observed in similar UCr_4C_4 phosphors.[19,21] This fact might be linked to the rigid structure (we compute a Debye temperature of 878.5 K) that distributes the local strain caused by the localized 5d−4f excitation to atoms far from the Eu activator. Quantitatively, 61% of the total mass-weighted displacements $\Delta Q = \sqrt{\sum_\kappa M_\kappa \Delta R_\kappa^2}$ is contained in the Eu−N_8 cuboid for Eu(Sr1) and 50% is contained for Eu(Sr2). Given the high Eu mass, the Eu atom contributes to this ΔQ up to 49% in Eu(Sr1) and up to 30% in Eu(Sr2).

By closely inspecting the difference between Eu(Sr1) and Eu(Sr2), we observe that a main relaxation pattern in Eu(Sr1) is a long-range displacement of the Sr chain, as already observed in $Sr[Li_2Al_2O_2N_2]:Eu^{2+}$, which is a consequence of the $5d_{z^2}$ orientation along this chain. Given the high Sr mass, we expect that the Sr displacements are predominant in shaping the electron−phonon spectral function of Eu(Sr1), as will be seen later. For Eu(Sr2), a major fraction of the displacements are distributed on the adjacent $[LiN_4]^{11-}$ and $[AlN_4]^{9-}$ tetrahedra, which is a consequence of the $5d_{x^2-y^2}$ lobes pointing toward it. We provide the structural parameters for pristine SLA, doped SLA Eu(Sr1), and doped SLA Eu(Sr2) in their 4f and 5d states in Table S1−S3 of the SI.[36] Finally, the energy between the computed relaxed excited and ground states provides an estimation of the ZPL energies, $E^{\text{ZPL-Sr1}}$ = 1.916 eV and $E^{\text{ZPL-Sr2}}$ = 1.989 eV, close to the experimental ZPL energies of 1.906 and 1.956 eV, respectively. In order to explain this difference in ZPL energies, one might invoke the difference in EuN_8 cuboid volumes between the two sites, as was done in ref 5 to explain the variation of emission energies across different oxy-nitrides and alkali lithosilicates. However, the very small difference between the two cuboid volumes (≈1%) is not sufficient for explaining the difference in ZPL energies. We believe that the different degrees of ionicity experienced by the 5d orbital due to the different numbers of $[LiN_4]^{11-}$ and $[AlN_4]^{9-}$ tetrahedra are responsible for the difference in ZPL energies. As a rough estimate, Eu(Sr1) with 3 $[LiN_4]^{11-}$ and 5 $[AlN_4]^{9-}$ has a second-shell formal charge of −78 e, while Eu(Sr2) with 1 $[LiN_4]^{11-}$ and 7 $[AlN_4]^{9-}$ has a second-shell formal charge of −74 e, where e is the absolute value of the electron charge. In SALON, this second-shell formal charge is −64 e. This is in line with the experimental ZPL energies of 1.906, 1.956, and 2.03 eV,[52] respectively.

Huang−Rhys Spectral Function. The Huang−Rhys spectral decomposition is presented in Figure 4. Equation 5 was used with a supercell containing 2304 atoms (4 × 4 × 4 supercell) thanks to the embedding procedure described in the theoretical section, which allows us to reach the dilute limit while keeping local and quasi-local modes caused by the Eu defect. The localization of the phonon modes can be characterized by computing the inverse participation ratio (IPR) defined as[14,15,21]

$$\text{IPR}_\nu = \frac{1}{\sum_\kappa |\langle \mathbf{e}_{\nu,\kappa} | \mathbf{e}_{\nu,\kappa} \rangle|^2} \tag{10}$$

which indicates, roughly speaking, the number of atoms that participate in a phonon mode ν. For example, $\text{IPR}_\nu = 1$ means that only one atom vibrates and therefore the phonon mode is maximally localized, while $\text{IPR}_\nu = N$ means that N atoms vibrate in the supercell with the same amplitude. The localization ratio β_ν is defined by taking the ratio of the total number of atoms in the supercell N and the IPR, $\beta_\nu = N/\text{IPR}_\nu$, where $\beta_\nu \approx 1$ represents a bulk-like delocalized mode and $\beta_\nu \gg 1$ corresponds to a quasi-local or local mode. We show in

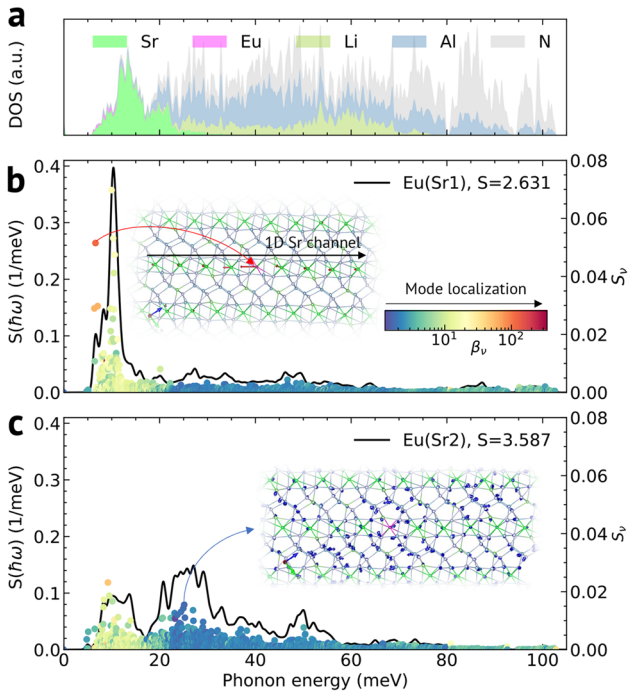

Figure 4. Spectral decomposition of the Huang−Rhys function obtained from the S_ν (colored dots), $S(\hbar\omega) = \sum_\nu S_\nu \delta(\hbar\omega - \hbar\omega_\nu)$ (black lines), using a 1 meV Gaussian broadening for both sites. (a) The atom-projected phonon density of states. The height of the dots, in (b) for Eu(Sr1) and (c) for Eu(Sr2), provides the partial Huang−Rhys factor of each phonon mode, while the color indicates the degree of localization of each mode β_ν (see text). For each Sr site, two illustrative modes with high Huang−Rhys factors but different degrees of localization are shown.

https://doi.org/10.1021/acs.chemmater.3c00537
Chem. Mater. 2023, 35, 5353−5361

Figure 4b and c the color-coded mode localization β_ν, which, combined with the atom-projected phonon density of states in Figure 4a, shows that the low-energy modes are more localized and dominate the electron−phonon coupling associated with the 5d−4f transition in the case of Eu(Sr1).

For Eu(Sr1), the spectral function is dominated by a large peak around 10 meV, where low-frequency phonon modes associated with Sr and Eu displacements are involved. They mostly correspond to long-wavelength collective displacements of the Sr atoms along the Sr chain that couple strongly with the 5d−4f relaxation of the Sr channel containing Eu described above. We compute a total Huang−Rhys factor $S = \sum_\nu S_\nu$ of 2.631 in that case and find that the phonons with a high partial HR factor S_ν can be either relatively delocalized or very localized. For instance, the highest coupling mode at 9.97 meV with $S_\nu = 0.07$ has a β_ν of 23. This mode is associated with the collective displacements of all the Sr atoms in the chain and can be considered as a slightly perturbed bulk mode. In contrast, the third highest coupling mode at 6.6 meV is very localized, with a $S_\nu = 0.05$ and a large β_ν of 115. As illustrated in the inset of Figure 4b, the atomic vibrations associated with this mode (red arrows) are localized around the Eu doping atom.

In the case of the second site Eu(Sr2), the spectral function indicates that phonon modes involving Eu and Sr atoms participate, but to a lesser extent than in the Eu(Sr1) case. Additionally, a broad peak appears between 20 and 40 meV, which is associated with modes involving Al and N atoms. The total Huang−Rhys factor of 3.587 indicates stronger electron−phonon coupling. The highest coupling mode located at 9.2 meV with $S_\nu = 0.023$ has a β_ν of 59. This mode is mostly associated with the Eu atom moving in its cage. Similarly to the Eu(Sr1) case, there are also a number of delocalized bulk modes that contribute. Indicatively, the fifth highest coupling mode at 25.1 meV with a $S_\nu = 0.015$ has a β_ν of 1.7 and is illustrated in the inset of Figure 4c. The atomic vibrations associated with this mode (blue arrows) are distributed mainly on Al and N atoms in the whole system. We analyze in detail the five phonon modes which contribute the most to the spectral function in Section 7 of the SI.[36]

Photoluminescence Spectrum and Its Temperature Dependence. Using the generating function approach described in the theoretical section, we computed the photoluminescence (PL) intensity from the Huang−Rhys spectral function. Figure 5 compares the PL spectra from both sites at 0 K with the experimental PL intensities at 10 K from ref 26, where the total PL intensity was deconvoluted with time-resolved spectroscopy (red and blue dotted curves). The total spectrum is also in good agreement with prior measurements at 6 K.[7]

For definitiveness, we have (i) aligned our computed ZPL energy of Eu(Sr1) with the highest experimental peak,[26] (ii) used a constant Lorentzian broadening of 25 meV, and (iii) used the experimental Eu(Sr1) to Eu(Sr2) total intensity ratio (computed as the ratio between the areas under the curves) from ref 26. We do not attempt in this work to compute these weights from first principles, which would require us to correctly compare the energetics and the electric dipole matrix elements of both sites. Indeed, the weight of the second PL intensity (ZPL at 1.956 eV) is different between the two experiments, which could be explained by different synthesis conditions. We note also that the energy difference between the experimental ZPL energies is 50 meV while the computed

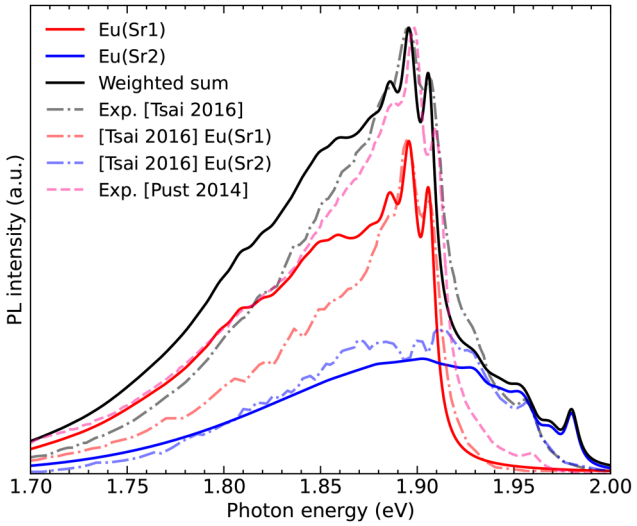

Figure 5. Computed photoluminescence intensities $L(\hbar\omega)$ for both Sr sites at 0 K and their weighted sum compared with two low-temperature experiments.[7,26] The red and blue dotted curves are experimental PL intensities of both sites from ref 26, where the total PL intensity (gray dotted curve) was deconvoluted with time-resolved spectroscopy. The computed Eu(Sr1) zero-phonon line energy is aligned with the second highest peak of the experimental data from ref 26, and the two weights for the black line are also taken from ref 26. Reproduced with permission from refs 7 and 26. Copyright 2014 Springer Nature and 2016 John Wiley and Sons.

energy difference is 74 meV. This explains the misalignment observed in Figure 5 between the experimental and the computed Eu(Sr2) ZPL.

The vibronic peaks appearing in the experimental spectra as well as the global shapes of both spectra match our computations, which means that the sharper PL spectrum with ZPL at 1.906 eV can be assigned with confidence to the Sr1 site while the broader spectrum with ZPL at 1.956 eV can be assigned to the Sr2 site. When looking at the total experimental spectrum, the high-energy peak at 1.956 eV can be assigned to the ZPL of the Eu(Sr2) center, the peak at 1.906 eV to the ZPL of the Eu(Sr1) center, and the next two peaks to the one- and two-phonon contributions of strontium-based phonon modes in Eu(Sr1). We still note that our computed total Huang−Rhys factor for Eu(Sr1) S_1 seems slightly overestimated. In order to estimate the experimental S_1, the 5d−4f forces can be scaled to fit the experimental spectrum. Scaling the forces by 90% (giving $S_1^{\mathrm{exp}} \approx 2.13$) allows one to obtain an excellent reproduction of the experimental phonon sideband (figure S11).

Finally, all the elements can be placed together to compute the temperature-dependent PL spectrum of SLA using eq 2, which we present in Figure 6a. This achievement represents the main result of our work with excellent experimental agreement. The effect of thermal expansion on the ZPL energy is quite similar for Eu(Sr1) and Eu(Sr2) and leads to a blue shift of 29 and 32 meV from 0 to 573 K, respectively (see Figure 6b). The ZPL shifts associated with the zero-point volume for both sites are estimated to be 21 and 25 meV, respectively. With increasing temperature, the spectrum broadens, with a progressive loss of clear vibronic peaks.

Figure 6c presents the position of the emission maximum as a function of temperature, with and without accounting for thermal expansion. When thermal expansion is not considered,

https://doi.org/10.1021/acs.chemmater.3c00537
Chem. Mater. 2023, 35, 5353−5361

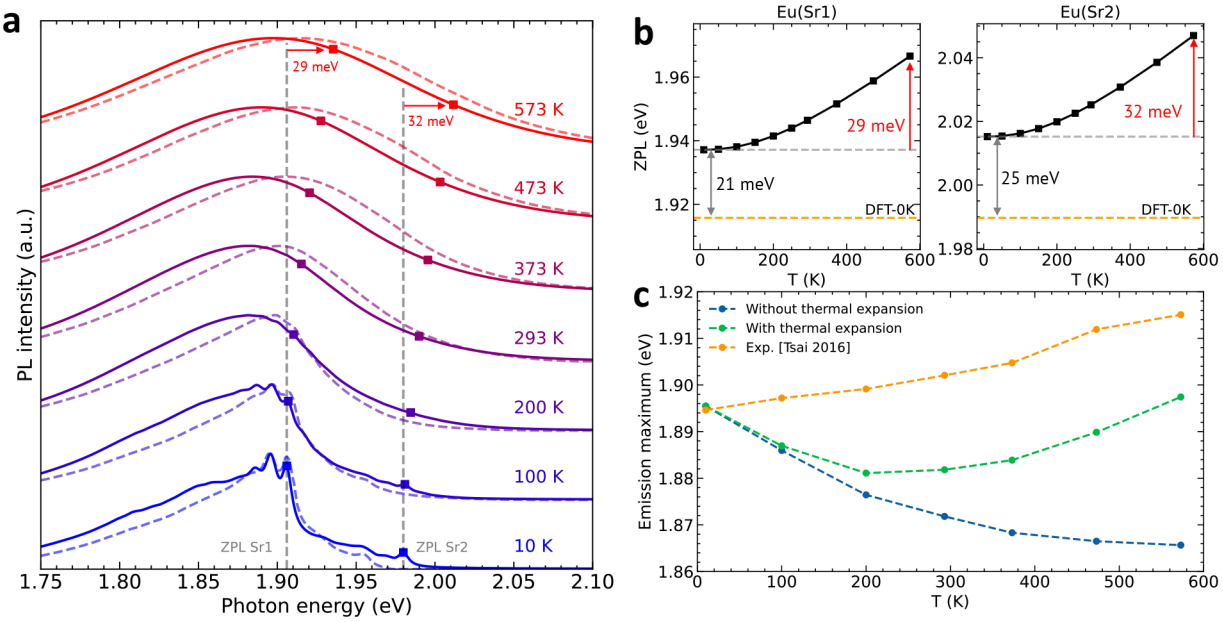

Figure 6. (a) Temperature-dependent photoluminescence (PL) spectrum computed with eq 2 (plain curves) and compared with experimental data[26] (dashed curves). The zero-phonon line (ZPL) energies at 0 K are indicated by gray vertical dashed lines, and the ZPL energies including thermal expansion effects are indicated with squares. The PL spectra for each temperature are shifted vertically for clarity. (b) Effect of thermal expansion on the ZPL energies for both sites; the DFT values at 0 K are shown with horizontal orange dashed lines. The shifts associated with the zero-point volume for Eu(Sr1) and Eu(Sr2) are 21 and 25 meV, respectively. Between 0 and 573 K, thermal expansion leads to a blue shift of 29 and 32 meV, respectively. (c) Photon energy of the emission maximum as a function of temperature. Ignoring thermal expansion leads to a red shift in the emission maximum. Adding the thermal expansion effect allows for a better agreement with the experiment.

a red shift between 10 and 573 K is computed. This is attributed to the positioning of the vibronic transitions that are activated by temperature relative to the emission maximum. Above 200 K, where the position of the emission maximum is determined by the envelope of the vibronic transitions, accounting for thermal expansion yields the temperature dependence observed experimentally. We notice that the ω^3 dependence of $L(\hbar\omega) \propto \omega^3 A(\hbar\omega)$ causes a blue shift of the emission maximum due to the broadening of the line shape function $A(\hbar\omega)$ with temperature, even if $A(\hbar\omega)$ does not shift. This leads to a blue shift of +11 meV between 0 and 573 K (see Section 9.2 of the SI). We provide the site decomposition of this emission maximum shift and further details in the SI.[36] Our analysis sheds new light on the puzzling phenomenon of the temperature-induced shift in phosphor materials, which remains theoretically underexplored.[53,54] It highlights the importance of both the ω^3 dependence of the PL intensity and the effect of thermal expansion.

CONCLUSIONS

In this work, the vibronic processes occurring in the narrow band emission $SrLiAl_3N_4:Eu^{2+}$ red phosphor are characterized from first principles. Two Sr sites can host the Eu activator, leading to two emission centers. The first, denoted as Sr1, is surrounded by 3 $[LiN_4]^{11-}$ and 5 $[AlN_4]^{9-}$ tetrahedra, while the second, denoted as Sr2, is surrounded by 1 $[LiN_4]^{11-}$ and 7 $[AlN_4]^{9-}$ tetrahedra. We apply the ΔSCF-constrained method to optimize Eu 5d excited state structures for both sites, independently. Different 5d orbitals are stabilized: a $5d_{z^2}$-like state aligned along the Sr channel for Eu(Sr1) and a $5d_{x^2-y^2}$-like state pointing along Al/Li atoms for Eu(Sr2).

The 5d−4f atomic relaxation is dominated by a long-range displacement of the Sr chain for Eu(Sr1), as a consequence of the $5d_{z^2}$ orientation. By projecting the atomic relaxation onto the phonon modes of a large doped supercell, we identify the phonon that couples the most with the 5d−4f transition. For Eu(Sr1), low-frequency phonon modes associated with Sr and Eu displacements are involved. They correspond either to bulk-like collective displacements of the Sr chains or to very localized modes concentrated on the Sr chain around the Eu activator. We computed a total Huang−Rhys factor of S = 2.631 resulting in a small coupling with phonons of low frequency which yields a small bandwidth. The same situation was found in $Sr[Li_2Al_2O_2N_2]:Eu^{2+}$, suggesting that the small bandwidth of other UCr_4C_4-type phosphors with the Ca/Sr/Ba channel can be explained in a similar way. For Eu(Sr2), as a consequence of a different 5d orbital orientation, modes associated with Sr and Eu displacements are less involved, and delocalized bulk modes involving Al and N atoms contribute as well, leading to a higher Huang−Rhys factor of S = 3.587. This larger coupling with phonons of higher frequencies yields a broader line shape. By comparing our computations with experimental low-temperature photoluminescent spectra, we are able to assign the peak at 1.906 eV to the ZPL of the Eu(Sr1) center and the next two peaks at 1.89 and 1.88 eV to the one- and two-phonon contributions of strontium-based phonon modes, respectively. The peak at 1.956 eV is assigned to the ZPL of the Eu(Sr2) center. Finally, we show the importance of the thermal expansion effect on the ZPL energies, which induces a blue shift of around 30 meV for both sites between 10 and 573 K. This results in a good agreement between our simulated temperature-dependent PL spectra and the experimental data for both the broadening and the shift of the spectrum with temperature. Overall, this work offers a direct theoretical understanding of the observed spectrum of $SrLiAl_3N_4:Eu^{2+}$ that highlights the importance of the Sr

https://doi.org/10.1021/acs.chemmater.3c00537
Chem. Mater. 2023, 35, 5353−5361

channels in shaping the small bandwidth. These findings are general and should apply to any UCr_4C_4-type phosphors.

■ ASSOCIATED CONTENT

Supporting Information

The Supporting Information is available free of charge at https://pubs.acs.org/doi/10.1021/acs.chemmater.3c00537.

Details on the embedding approach, influence of the Hubbard *U*, phonon band structure of pristine SLA, additional details on thermal expansion, additional details on structural parameters, Kohn−Sham levels, dominant phonon modes, Eu(Sr1) PL spectrum with scaled forces, and additional details on the emission shift with temperature (PDF)

■ AUTHOR INFORMATION

Corresponding Author

Julien Bouquiaux − *Institute of Condensed Matter and Nanosciences, Université catholique de Louvain, B-1348 Louvain-la-Neuve, Belgium;* orcid.org/0000-0003-1982-052X; Email: julien.bouquiaux@uclouvain.be

Authors

Samuel Poncé − *Institute of Condensed Matter and Nanosciences, Université catholique de Louvain, B-1348 Louvain-la-Neuve, Belgium*

Yongchao Jia − *Yanshan University, Hebei Key Laboratory of Applied Chemistry, Yanshan University, 066004 Qinhuangdao, P. R. China*

Anna Miglio − *Institute of Condensed Matter and Nanosciences, Université catholique de Louvain, B-1348 Louvain-la-Neuve, Belgium*

Masayoshi Mikami − *Materials Design Laboratory, Science & Innovation Center, Mitsubishi Chemical Corporation, Yokohama 227-8502, Japan*

Xavier Gonze − *Institute of Condensed Matter and Nanosciences, Université catholique de Louvain, B-1348 Louvain-la-Neuve, Belgium;* orcid.org/0000-0002-8377-6829

Complete contact information is available at: https://pubs.acs.org/10.1021/acs.chemmater.3c00537

Notes

The authors declare no competing financial interest.

■ ACKNOWLEDGMENTS

Computational resources have been provided by the supercomputing facilities of the Université catholique de Louvain (CISM/UCL) and the Consortium des Équipements de Calcul Intensif en Fédération Wallonie Bruxelles (CÉCI) funded by the Fond de la Recherche Scientifique de Belgique (F.R.S.-FNRS) under convention 2.5020.11 and by the Walloon Region, as well as the Tier-1 supercomputer of the Fédération Wallonie-Bruxelles, infrastructure funded by the Walloon Region underGrant Agreement 1117545. We thank the Consortium des Équipements de Calcul Intensif, Belgium for awarding this project access to the LUMI supercomputer, owned by the EuroHPC Joint Undertaking, hosted by CSC (Finland) and the LUMI consortium through Project 465000061. J.B. and S.P. acknowledge support from the F.R.S.-FNRS. X.G. also acknowledges support from the F.R.S.-FNRS, under Grant T.0103.19 (PDR-ALPS). This work was supported by the Communauté française de Belgique through the SURFASCOPE project (ARC 19/24-102). Y.J. acknowledges the funding support from the National Key R&D Program (2022YFB3503800), the Natural Science Foundation of Hebei Province (E2021203126), and the Cultivation Project for Basic Research and Innovation of Yanshan University (2021LGQN033).

■ REFERENCES

(1) Lin, C. C.; Meijerink, A.; Liu, R.-S. Critical red components for next-generation white LEDs. *journal of physical chemistry letters* **2016**, *7*, 495−503.

(2) Pust, P.; Schmidt, P. J.; Schnick, W. A revolution in lighting. *Nature materials* **2015**, *14*, 454−458.

(3) Lee, K. *2022 Solid-State Lighting R&D Opportunities*; 2022, DOI: 10.2172/1862626

(4) Fang, M.-H.; Bao, Z.; Huang, W.-T.; Liu, R.-S. Evolutionary generation of phosphor materials and their progress in future applications for light-emitting diodes. *Chem. Rev.* **2022**, *122*, 11474−11513.

(5) Fang, M.-H.; Mariano, C. O. M.; Chen, P.-Y.; Hu, S.-F.; Liu, R.-S. Cuboid-size-controlled color-tunable Eu-doped alkali-lithosilicate phosphors. *Chem. Mater.* **2020**, *32*, 1748−1759.

(6) Fang, M.-H.; Leaño, J. L., Jr; Liu, R.-S. Control of narrow-band emission in phosphor materials for application in light-emitting diodes. *ACS Energy Letters* **2018**, *3*, 2573−2586.

(7) Pust, P.; Weiler, V.; Hecht, C.; Tücks, A.; Wochnik, A. S.; Henß, A.-K.; Wiechert, D.; Scheu, C.; Schmidt, P. J.; Schnick, W. Narrow-band red-emitting $Sr[LiAl_3N_4]$: Eu^{2+} as a next-generation LED-phosphor material. *Nature materials* **2014**, *13*, 891−896.

(8) Pust, P.; Hintze, F.; Hecht, C.; Weiler, V.; Locher, A.; Zitnanska, D.; Harm, S.; Wiechert, D.; Schmidt, P. J.; Schnick, W. Group (III) Nitrides $M[Mg_2Al_2N_4]$(M= Ca, Sr, Ba, Eu) and $Ba[Mg_2Ga_2N_4]$-Structural Relation and Nontypical Luminescence Properties of Eu^{2+} Doped Samples. *Chem. Mater.* **2014**, *26*, 6113−6119.

(9) Schmiechen, S.; Schneider, H.; Wagatha, P.; Hecht, C.; Schmidt, P. J.; Schnick, W. Toward new phosphors for application in illumination-grade white pc-LEDs: the nitridomagnesosilicates Ca-$[Mg_3SiN_4]$: Ce^{3+}, $Sr[Mg_3SiN_4]$: Eu^{2+}, and $Eu[Mg_3SiN_4]$. *Chem. Mater.* **2014**, *26*, 2712−2719.

(10) Hoerder, G. J.; Seibald, M.; Baumann, D.; Schröder, T.; Peschke, S.; Schmid, P. C.; Tyborski, T.; Pust, P.; Stoll, I.; Bergler, M.; et al. $Sr[Li_2Al_2O_2N_2]$:Eu^{2+}—A high performance red phosphor to brighten the future. *Nat. Commun.* **2019**, *10*, 1−9.

(11) Zhao, M.; Liao, H.; Ning, L.; Zhang, Q.; Liu, Q.; Xia, Z. Next-generation narrow-band green-emitting $RbLi(Li_3SiO_4)_2$:Eu^{2+} phosphor for backlight display application. *Adv. Mater.* **2018**, *30*, 1802489.

(12) Liao, H.; Zhao, M.; Molokeev, M. S.; Liu, Q.; Xia, Z. Learning from a mineral structure toward an ultra-narrow-band blue-emitting silicate phosphor $RbNa_3(Li_3SiO_4)_4$:Eu^{2+}. *Angew. Chem.* **2018**, *130*, 11902−11905.

(13) Huang, K.; Rhys, A. Theory of light absorption and non-radiative transitions in F-centres. *Proceedings of the Royal Society of London. Series A. Mathematical and Physical Sciences* **1950**, *204*, 406−423.

(14) Alkauskas, A.; Buckley, B. B.; Awschalom, D. D.; Van de Walle, C. G. First-principles theory of the luminescence lineshape for the triplet transition in diamond NV centres. *New J. Phys.* **2014**, *16*, 073026.

(15) Jin, Y.; Govoni, M.; Wolfowicz, G.; Sullivan, S. E.; Heremans, F. J.; Awschalom, D. D.; Galli, G. Photoluminescence spectra of point defects in semiconductors: Validation of first-principles calculations. *Physical Review Materials* **2021**, *5*, 084603.

(16) Linderälv, C.; Wieczorek, W.; Erhart, P. Vibrational signatures for the identification of single-photon emitters in hexagonal boron nitride. *Phys. Rev. B* **2021**, *103*, 115421.

(17) Gali, Á. Ab initio theory of the nitrogen-vacancy center in diamond. *Nanophotonics* **2019**, *8*, 1907−1943.

(18) Razinkovas, L.; Doherty, M. W.; Manson, N. B.; Van de Walle, C. G.; Alkauskas, A. Vibrational and vibronic structure of isolated point defects: The nitrogen-vacancy center in diamond. *Phys. Rev. B* **2021**, *104*, 045303.
(19) Bouquiaux, J.; Poncé, S.; Jia, Y.; Miglio, A.; Mikami, M.; Gonze, X. Importance of Long-Range Channel Sr Displacements for the Narrow Emission in $Sr[Li_2Al_2O_2N_2]:Eu^{2+}$ Phosphor. *Advanced Optical Materials* **2021**, *9*, 2100649.
(20) Linderälv, C.; Åberg, D.; Erhart, P. Luminescence quenching via deep defect states: A recombination pathway via oxygen vacancies in Ce-doped YAG. *Chem. Mater.* **2021**, *33*, 73−80.
(21) Wang, X.; Huang, X.; Zhao, M.; Tanner, P. A.; Zhou, X.; Ning, L. Role of the Rigid Host Structure in Narrow-Band Green Emission of Eu^{2+} in $Rb_2Na_2(Li_3SiO_4)_4$: Insights into Electron-Phonon Coupling. *Inorg. Chem.* **2022**, *61*, 7617−7623.
(22) Wang, L.; Xie, R.-J.; Suehiro, T.; Takeda, T.; Hirosaki, N. Down-conversion nitride materials for solid state lighting: recent advances and perspectives. *Chem. Rev.* **2018**, *118*, 1951−2009.
(23) Tolhurst, T. M.; Boyko, T. D.; Pust, P.; Johnson, N. W.; Schnick, W.; Moewes, A. Investigations of the Electronic Structure and Bandgap of the Next-Generation LED-Phosphor $SrLiAl_3N_4:Eu^{2+}$—Experiment and Calculations. *Advanced Optical Materials* **2015**, *3*, 546−550.
(24) Tolhurst, T. M.; Schmiechen, S.; Pust, P.; Schmidt, P. J.; Schnick, W.; Moewes, A. Electronic structure, bandgap, and thermal quenching of $Sr[Mg_3SiN_4]:Eu^{2+}$ in comparison to $Sr[LiAl_3N_4]:Eu^{2+}$. *Advanced Optical Materials* **2016**, *4*, 584−591.
(25) Shafei, R.; Maganas, D.; Strobel, P. J.; Schmidt, P. J.; Schnick, W.; Neese, F. Electronic and optical properties of Eu^{2+}-activated narrow-band phosphors for phosphor-converted light-emitting diode applications: Insights from a theoretical spectroscopy perspective. *J. Am. Chem. Soc.* **2022**, *144*, 8038−8053.
(26) Tsai, Y.-T.; Nguyen, H.-D.; Lazarowska, A.; Mahlik, S.; Grinberg, M.; Liu, R.-S. Improvement of the Water Resistance of a Narrow-Band Red-Emitting $SrLiAl_3N_4:Eu^{2+}$ Phosphor Synthesized under High Isostatic Pressure through Coating with an Organosilica Layer. *Angew. Chem., Int. Ed.* **2016**, *55*, 9652−9656.
(27) Jia, Y.; Miglio, A.; Poncé, S.; Gonze, X.; Mikami, M. First-principles study of Ce^{3+}-doped lanthanum silicate nitride phosphors: Neutral excitation, Stokes shift, and luminescent center identification. *Phys. Rev. B* **2016**, *93*, 155111.
(28) Poncé, S.; Jia, Y.; Giantomassi, M.; Mikami, M.; Gonze, X. Understanding thermal quenching of photoluminescence in oxy-nitride phosphors from first principles. *J. Phys. Chem. C* **2016**, *120*, 4040−4047.
(29) Jia, Y.; Miglio, A.; Poncé, S.; Mikami, M.; Gonze, X. First-principles study of the luminescence of Eu^{2+}-doped phosphors. *Phys. Rev. B* **2017**, *96*, 125132.
(30) Jia, Y.; Poncé, S.; Miglio, A.; Mikami, M.; Gonze, X. Assessment of first-principles and semiempirical methodologies for absorption and emission energies of Ce^{3+}-doped luminescent materials. *Advanced Optical Materials* **2017**, *5*, 1600997.
(31) Jia, Y.; Poncé, S.; Miglio, A.; Mikami, M.; Gonze, X. Design rule for the emission linewidth of Eu^{2+}-activated phosphors. *J. Lumin.* **2020**, *224*, 117258.
(32) Rignanese, G.-M.; Michenaud, J.-P.; Gonze, X. Ab initio study of the volume dependence of dynamical and thermodynamical properties of silicon. *Phys. Rev. B* **1996**, *53*, 4488.
(33) Carrier, P.; Wentzcovitch, R.; Tsuchiya, J. First-principles prediction of crystal structures at high temperatures using the quasiharmonic approximation. *Phys. Rev. B* **2007**, *76*, 064116.
(34) Lax, M. The Franck-Condon principle and its application to crystals. *J. Chem. Phys.* **1952**, *20*, 1752−1760.
(35) Kubo, R.; Toyozawa, Y. Application of the method of generating function to radiative and non-radiative transitions of a trapped electron in a crystal. *Prog. Theor. Phys.* **1955**, *13*, 160−182.
(36) See the Supporting Information.
(37) Gonze, X.; et al. First-principles computation of material properties: the ABINIT software project. *Comput. Mater. Sci.* **2002**, *25*, 478−492.
(38) Gonze, X.; et al. The ABINIT project: Impact, environment and recent developments. *Comput. Phys. Commun.* **2020**, *248*, 107042.
(39) Torrent, M.; Jollet, F.; Bottin, F.; Zérah, G.; Gonze, X. Implementation of the projector augmented-wave method in the ABINIT code: Application to the study of iron under pressure. *Comput. Mater. Sci.* **2008**, *42*, 337−351.
(40) Perdew, J. P.; Burke, K.; Ernzerhof, M. Generalized gradient approximation made simple. *Phys. Rev. Lett.* **1996**, *77*, 3865.
(41) Joos, J. J.; Smet, P. F.; Seijo, L.; Barandiarán, Z. Insights into the complexity of the excited states of Eu-doped luminescent materials. *Inorganic Chemistry Frontiers* **2020**, *7*, 871−888.
(42) Barandiarán, Z.; Joos, J.; Seijo, L. *Luminescent Materials: A Quantum Chemical Approach for Computer-Aided Discovery and Design*; 2022, *322*.
(43) Gonze, X.; Lee, C. Dynamical matrices, Born effective charges, dielectric permittivity tensors, and interatomic force constants from density-functional perturbation theory. *Phys. Rev. B* **1997**, *55*, 10355.
(44) Togo, A.; Tanaka, I. First principles phonon calculations in materials science. *Scripta Materialia* **2015**, *108*, 1−5.
(45) Carrier, P.; Justo, J. F.; Wentzcovitch, R. M. Quasiharmonic elastic constants corrected for deviatoric thermal stresses. *Phys. Rev. B* **2008**, *78*, 144302.
(46) Allan, N.; Barron, T.; Bruno, J. The zero static internal stress approximation in lattice dynamics, and the calculation of isotope effects on molar volumes. *J. Chem. Phys.* **1996**, *105*, 8300−8303.
(47) Masuki, R.; Nomoto, T.; Arita, R.; Tadano, T. Full optimization of quasiharmonic free energy with anharmonic lattice model: Application to thermal expansion and pyroelectricity of wurtzite GaN and ZnO. *arXiv preprint arXiv:2302.04537* **2023**, DOI: 10.1103/PhysRevB.107.134119.
(48) Ritz, E. T.; Li, S. J.; Benedek, N. A. Thermal expansion in insulating solids from first principles. *J. Appl. Phys.* **2019**, *126*, 171102.
(49) Brousseau-Couture, V.; Godbout, É.; Côté, M.; Gonze, X. Zero-point lattice expansion and band gap renormalization: Grüneisen approach versus free energy minimization. *Phys. Rev. B* **2022**, *106*, 085137.
(50) Fu, C.-L.; Ho, K.-M. First-principles calculation of the equilibrium ground-state properties of transition metals: Applications to Nb and Mo. *Phys. Rev. B* **1983**, *28*, 5480.
(51) Shannon, R. D. Revised effective ionic radii and systematic studies of interatomic distances in halides and chalcogenides. *Acta crystallographica section A: crystal physics, diffraction, theoretical and general crystallography* **1976**, *32*, 751−767.
(52) Ruegenberg, F.; García-Fuente, A.; Seibald, M.; Baumann, D.; Hoerder, G.; Fiedler, T.; Urland, W.; Huppertz, H.; Meijerink, A.; Suta, M. Mixed Microscopic Eu^{2+}Occupancies in the Next-Generation Red LED Phosphor $Sr[Li_2Al_2O_2N_2]:{}^{2+}$ (SALON:Eu^{2+}). *Advanced Optical Materials* **2023**, *11*, 2202732.
(53) Yan, S. On the origin of temperature dependence of the emission maxima of Eu^{2+} and Ce^{3+}-activated phosphors. *Opt. Mater.* **2018**, *79*, 172−185.
(54) Xu, J.; Huang, X.; Cheng, X.; Whangbo, M.-H.; Deng, S. Microscopic Mechanism of the Heat-Induced Blueshift in Phosphors and a Logarithmic Energy Dependence on the Nearest Dopant-Vacancy Distance. *Angew. Chem., Int. Ed.* **2022**, *61*, No. e202116404.

https://doi.org/10.1021/acs.chemmater.3c00537
Chem. Mater. 2023, 35, 5353−5361